International Journal on Magnetic Particle Imaging
Vol 3, No 1, Article ID 1703011, 9 Pages

Infinite Science Publishing

Research Article

Submillimeter-Accurate Marker Localization within Low Gradient Magnetic Particle Imaging Tomograms

Florian Griese[a,*] · Tobias Knopp[a] · René Werner[b] · Alexander Schlaefer[c] · Martin Möddel[a]

[a] Section for Biomedical Imaging, University Medical Center Hamburg, Hamburg, Germany
[b] Section for Image Processing and Medical Informatics, University Medical Center Hamburg, Hamburg, Germany
[c] Institute of Medical Technology, Hamburg University of Technology, Germany
[*] Corresponding author, email: f.griese@uke.de

Received 29 November 2016; Accepted 21 February 2017; Published online 23 March 2017

Abstract

Magnetic Particle Imaging (MPI) achieves a high temporal resolution, which opens up a wide range of real-time medical applications such as device tracking and navigation. These applications usually rely on automated techniques for finding and localizing devices and fiducial markers in medical images. In this work, we show that submillimeter-accurate automatic marker localization from low gradient MPI tomograms with a spatial resolution of several millimeters is possible. Markers are initially identified within the tomograms by a thresholding-based segmentation algorithm. Subsequently, their positions are accurately determined by calculating the center of mass of the voxel intensities inside the pre-segmented regions. A series of phantom measurements taken at full temporal resolution (46 Hz) is used to analyze statistical and systematical errors and to discuss the performance and stability of the automatic submillimeter-accurate marker localization algorithm.

I. Introduction

Magnetic Particle Imaging (MPI) is a 3D tomographic imaging modality [1] visualizing the spatial distribution of superparamagnetic iron oxide nanoparticles (SPIOs). MPI has a high temporal resolution [2], a high sensitivity with a detection limit of few nanograms iron [3, 4], and is free of ionizing radiation. Besides oncological applications like cell tracking [4–6] the high imaging speed renders MPI promising for interventional applications, where nowadays the X-ray-based digital subtraction angiography (DSA) is the method of choice [7]. The suitability of MPI for interventional applications was examined in [8], where a catheter was coated with SPIOs and imaged in real-time with MPI. Dedicated real-time reconstruction algorithms were discussed in [9]. In [10], MPI was used for the treatment of stenosis in a vessel phantom, whereas in [11], it was shown that vessels and instruments can be separately visualized by applying multi-spectral imaging techniques [12].

Interventional applications, however, require accurate localization of (coated) medical instruments or fiducial markers [13]. One way to achieve this goal is to perform imaging with high spatial resolution, which in MPI mainly depends on the tracer performance and the gradient strength of the selection field. Tracer performance has improved significantly over the last years [14]. However, the resolution gain, which can be achieved using tailored MPI tracers, is limited by physical constraints [15, 16]. For high gradient fields in the range of 5.5 $\mathrm{T\,m^{-1}}$ to 7 $\mathrm{T\,m^{-1}}$, a spatial resolution higher than 1 mm has

been reported [17, 18]. Recent experimental setups even described gradient fields of up to 85 T m^{-1}, providing resolutions in μm range [19].

However, for clinical MPI scanners, the gradient strength of about 1 T m^{-1} to 3 T m^{-1} will be challenging to realize, at least for the current scanner designs, due to the electrical power loss of the field generating coils. A rough prediction of the achievable resolution has been given in [20], with a refinement proposed in [21]. But even 1 mm spatial resolution as achieved in [17] for 5.5 T m^{-1} still does not compete with spatial resolutions in DSA, making accurate instrument localization challenging.

In other imaging modalities such as CT and MRI, automated subpixel-accurate localization approaches have been successfully applied to circumvent this problem [22]. Thus, the purpose of this work is to analyze and illustrate feasibility of subpixel-accurate – i.e. in this case submillimeter-accurate – automatic marker localization in low spatial resolution MPI data. Therefore, a preclinical MPI scanner at full temporal resolution is used to mimic the scenario of labeled catheters within an interventional MPI setup.

II. Material and Methods

II.I. Experimental Setup

All MPI measurements are performed with a preclinical MPI scanner (Philips/Bruker). The scanner drives a field free point along a 3D Lissajous trajectory with drive field coils in x-, y-, and z-direction. The excitation of each coil is sinusoidal with an amplitude of 14 mT and frequencies of $f_x = 2.5/102$ MHz, $f_y = 2.5/96$ MHz, and $f_x = 2.5/99$ MHz, respectively. The chosen frequencies result in a cycle period length for a single frame of 21.54 ms and a respective imaging frame rate of 46.43 Hz. The selection field is set to a gradient of 1.5 T m^{-1} in z-direction and 0.75 T m^{-1} in x- and y-directions. With these parameters the Lissajous trajectory covers a drive field field of view of 37.3 mm × 37.3 mm × 18.7 mm.

Prior to reconstruction, a system matrix is acquired in a calibration scan. A 2 mm × 2 mm × 1 mm delta sample containing 4 µL ferucarbotran (Resovist, Irom Pharmaceuticals, Tokio, Japan) with an iron concentration of 83 mmol L^{-1} is moved to 20 × 20 × 20 equidistant positions in a 40 mm × 40 mm × 20 mm field of view. At each position, the response of the delta sample is recorded for 30 Lissajous cycles.

II.II. Image Reconstruction

3D MPI tomograms are reconstructed using the algebraic approach [23], where the system matrix $\boldsymbol{S}$ is measured using a delta sample. The voltages measured during the MPI experiments in the receive coils are Fourier transformed and frequencies below 80 kHz are discarded in a post processing step. This is because frequencies below 80 kHz carry unpredictable background signal that cannot be reliably subtracted for the MPI scanner considered in this work. In addition, we apply an SNR threshold of 3 to remove noisy system matrix rows using the frequency selection algorithm discussed in [17]. The frequency component vectors s_i of each position form the columns of the system function $\boldsymbol{S}$.

The MPI tomogram $\boldsymbol{I}$ can be obtained using a first-order Tikhonov-regularized least squares approach

$$\boldsymbol{I} = \underset{\zeta}{\operatorname{argmin}} \|\boldsymbol{S}\zeta - \hat{\boldsymbol{u}}\|_2^2 + \tilde{\lambda}\|\zeta\|_2^2, \tag{1}$$

where $\hat{\boldsymbol{u}}$ is the Fourier transform of measured time data $\boldsymbol{u}$. Instead of $\tilde{\lambda}$, one usually reports $\lambda = \frac{\tilde{\lambda}}{\lambda_0}$ where $\lambda_0 = \text{trace}(\boldsymbol{S}^*\boldsymbol{S})N^{-1}$ and N is the length of the vector ζ. The optimization problem (1) is solved in this work by the iterative Kaczmarz algorithm using 3 iterations. The influence of the regularization parameter λ can be seen in Fig. 1. When λ is chosen too small, artifacts appear in the image. Increasing λ reduces the artifacts but smoothes the data leading to a loss of resolution. For the considered data, we found that $\lambda = 0.01$ leads to a good compromise between a too noisy and an over-smoothed image.

We note that the spatial resolution in terms of the FWHM estimated from our data for $\lambda = 0.01$ is 6.3 mm, 8.0 mm, and 3.7 mm in x-, y-, and z-direction, respectively. This well agrees with the corresponding predicted values of 5.97 mm, 5.97 mm, and 2.99 mm when considering particles of 25 nm core diameter using the resolution formula introduced in [20]. Differences of x- and y-resolutions are related to the fact that our x- and y-receive channels have different characteristics, which influences the reconstruction process.

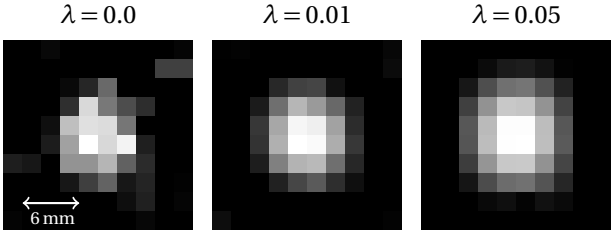

Figure 1: Influence of the regularization parameter λ on the reconstruction result. The delta sample is shown in cropped xy-slices within a 3D MPI tomogram with FOV of 37.3 mm × 37.3 mm × 18.7 mm. From left to right, the tomograms were reconstructed with regularization parameters $\lambda = 0$, 0.01, and 0.05. Without regularization (i.e. $\lambda = 0$), the image of the marker contains a lot of noise. The central image with $\lambda = 0.01$ provides a good compromise between noise reduction and spatial resolution. The right image contains nearly no noise but suffers from a loss of spatial resolution due to the over-regularization.

10.18416/ijmpi.2017.1703011

II.III. Automatic Marker Localization

In our setup, even small changes in the position of a marker lead to slight changes in the image intensities and their spatial distribution within the reconstructed tomograms as shown in Fig. 2. This motivates transferring established intensity-based subpixel-accurate marker detection approaches to the task at hand. In particular, we focus on and evaluate the well-known intensity centroiding approach that has been described to be successfully applied to various imaging modalities and (medical) applications [24, 25].

We consider a dynamic MPI experiment where $I : \Omega_s \times \mathbb{R} \to \mathbb{R}$ ($\Omega_s \subset \mathbb{R}^3$) represents the set of all MPI tomograms reconstructed from the dynamic measurement, i.e. $I(\boldsymbol{x}, t)$ represents the reconstructed particle concentration at spatial position $\boldsymbol{x}$ and time t. Then, the proposed automatic marker localization is performed in three steps. At first, a threshold filter is applied to each tomogram in order to separate markers (high image intensity structures) from background. This results in the data set $I^{\text{segBin}} : \Omega_s \times \mathbb{R} \to \mathbb{R}$ with

$$I^{\text{segBin}}(\boldsymbol{x}, t) = \begin{cases} 1 & \text{if } I(\boldsymbol{x}, t) \geq \Theta \cdot \max_{\boldsymbol{x}} I(\boldsymbol{x}, t) \\ 0 & \text{otherwise,} \end{cases} \tag{2}$$

where $\Theta \in [0, 1]$ denotes the relative threshold. The visualization of a filtered and unfiltered tomogram can be found in Fig. 3. The reference xy-slice is unfiltered, and the other images correspond to filtered versions of the same slice with relative thresholds of $\Theta = 0.1$, 0.3, 0.5, 0.7, and 1.0.

In a second step, connected regions $\Omega_l^t \subseteq \Omega_s$, $l \in \{1, 2, \ldots, L_t\}$ are identified by connected-component labeling of $I^{\text{segBin}}(\Omega_s, t)$, $t \in \mathbb{R}$. The regions are ordered with respect to the maximal intensity value within the region: $\max I(\Omega_1^t, t) \geq \max I(\Omega_2^t, t) \geq \cdots \geq \max I(\Omega_{L_t}^t, t)$.

Finally, it is assumed that $K < L_t$, where K is the number of markers, and the markers correspond to the first K ordered regions. The position of each of the K markers $1 \leq k \leq K$ is obtained by calculating the center of mass of the voxel intensities of the corresponding connected region in the MPI tomogram I

$$\boldsymbol{c}_k(t) = \frac{\int_{\Omega_k^t} \boldsymbol{x} \cdot I(\boldsymbol{x}, t) \mathrm{d}\boldsymbol{x}}{\int_{\Omega_k^t} I(\boldsymbol{x}, t) \mathrm{d}\boldsymbol{x}}. \tag{3}$$

II.IV. Evaluation

Let $\boldsymbol{r}_k : \mathbb{R} \to \mathbb{R}^3$ be the true position of marker k and t_i, $1 \leq i \leq N$ be the points in time for which a tomogram has been reconstructed. Then, the localization error $\boldsymbol{\delta}_k = (\delta_k^x, \delta_k^y, \delta_k^z)$ is given by the difference between true and calculated position

$$\boldsymbol{\delta}_k(t_i) = \boldsymbol{r}_k(t_i) - \boldsymbol{c}_k(t_i). \tag{4}$$

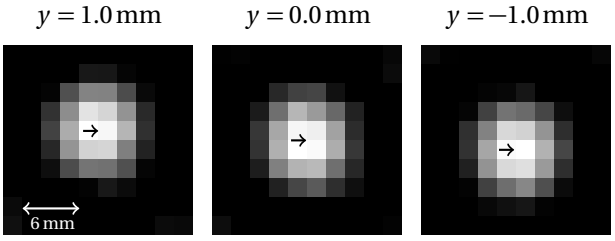

Figure 2: The delta sample is shown in cropped xy-slices within a 3D MPI tomogram with FOV of 37.3 mm × 37.3 mm × 18.7 mm. From left to right, the marker was positioned at $y = 1$ mm, 0 mm and −1 mm with fixed x- and z-position. Although each voxel has a length of 2 mm in y-direction, changes in the signal distribution within the gray scale images can be perceived.

In general, this error is the superposition of a statistical error and a systematic error; both of which may vary in time and depend on the spatial position.

To estimate the systematic error as a function of the marker position we average $\boldsymbol{\delta}_k$ for all $T_k^{\boldsymbol{x}} = \{t_i | \boldsymbol{r}_k(t_i) = \boldsymbol{x}\}$ to obtain

$$\mu_k^\alpha(\boldsymbol{x}) = \frac{1}{|T_k^{\boldsymbol{x}}|} \sum_{t \in T_k^{\boldsymbol{x}}} \delta_k^\alpha(t), \tag{5}$$

where $\alpha = x$, y, and z. The corresponding statistical error can be estimated by the spatially dependent standard deviation

$$\sigma_k^\alpha(\boldsymbol{x}) = \sqrt{\frac{1}{|T_k^{\boldsymbol{x}}|} \sum_{t \in T_k^{\boldsymbol{x}}} \left(\delta_k^\alpha(t) - \mu_k^\alpha(\boldsymbol{x})\right)^2}. \tag{6}$$

II.V. Sample Positioning

The preclinical MPI scanner used in this work is equipped with a 3 axes robot (Isel Automation GmbH). A 46.5 cm long fiberglas arm with diameter of 10 mm is mounted at the robot. At the tip of the arm, small tracer samples and other phantoms can be placed. The robot with the arm attached can be moved in three orthogonal directions (x, y, z) with a step size of 6.25 µm, allowing for precise and reproducible phantom placement during MPI measurements and for sampling the system matrix during the calibration procedure. The sample used during this calibration procedure is referred to as delta sample. Henceforth, all directions and coordinates will be provided in the robot coordinate system.

By using the calibration approach for image reconstruction, the image coordinate system and the robot coordinate system are automatically aligned. The origin of the robot coordinate system is set such that a 2 mm × 2 mm × 1 mm delta sample mounted at the tip of the arm is centered in the drive field field of view.

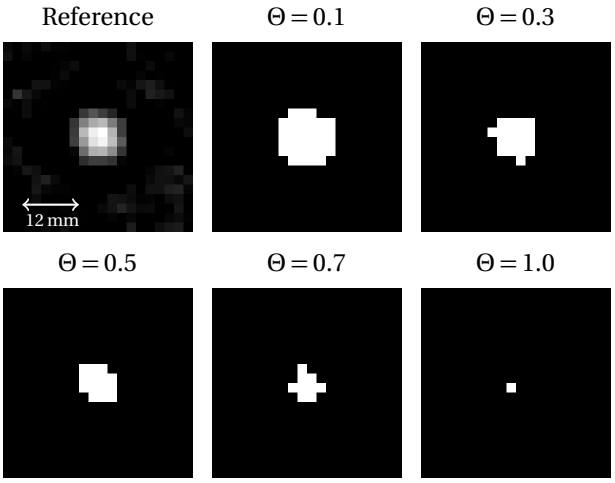

Figure 3: The delta sample is shown in *xy*-slices within a 3D MPI tomogram with FOV of 37.3 mm × 37.3 mm × 18.7 mm. Influence of the threshold Θ on the segmentation. The image in the top left corner is a reference tomogram obtained by reconstruction with $\lambda = 0.01$. All other images were obtained from the reference by applying a threshold filter with relative threshold Θ = 0.1, 0.3, 0.5, 0.7, and 1.0. For segmentation a threshold Θ of 0.3 was chosen.

II.VI. Marker Phantoms

We use two phantoms in our experiments. First, a single-marker-phantom consisting of the delta sample mounted at the tip of the robot arm. Throughout all experiments where the single-marker-phantom is used, the robot coordinates provide ground truth for the marker position.

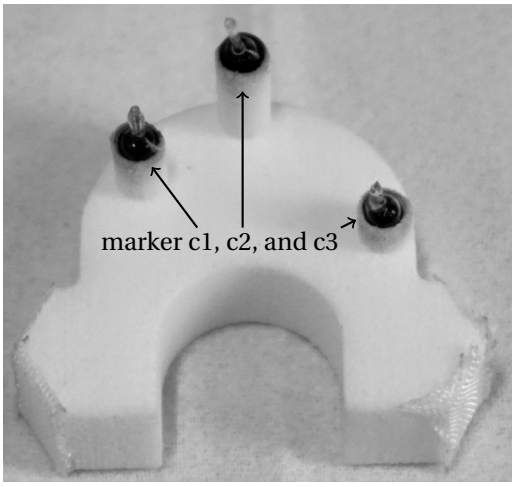

Figure 4: Multi-marker phantom, containing three markers in a triangular arrangement.

Besides the delta sample, we use a multi-marker phantom containing three markers (c1, c2, and c3) in a triangular arrangement as shown in Fig. 4. Each marker consists of a spherical sample of 2.85 mm diameter, containing 7.27 µL ferucarbotran with an iron concentration of 83 mmol L^{-1}. During measurement, the phantom is mounted on the robot arm. The center of mass locations $\boldsymbol{r}_1$, $\boldsymbol{r}_2$, and $\boldsymbol{r}_3$ of the markers c1-3 are unknown, but their respective distances $d_{12} = \|\boldsymbol{r}_1 - \boldsymbol{r}_2\|_2$, $d_{13} = \|\boldsymbol{r}_1 - \boldsymbol{r}_3\|_2$, an $d_{23} = \|\boldsymbol{r}_2 - \boldsymbol{r}_3\|_2$ can be estimated from the 3D CAD drawing of the phantom as listed in Tab. 1. Our estimation takes into account the 3D printing by selective laser sintering (SLS), which has a precision of ±0.1 mm, the manufacturing tolerance of the glass sphere holding the tracer, and the fixation error of spheres within the socket, which is negligible low.

Table 1: Distances between center positions known from model.

	$\boldsymbol{d}_{12}$	$\boldsymbol{d}_{13}$	$\boldsymbol{d}_{23}$
Distance [mm]	9.2 ± 0.3	17.3 ± 0.3	14.1 ± 0.3

II.VII. Experiments

To analyze feasibility and accuracy of the automated marker localization, we conduct a series of experiments using the single-marker-phantom. Additional experiments with the three-marker-phantom aimed to further illustrate feasibility of reliable marker identification and localization in more complex multi-marker arrangements.

For the first experiment the single-marker-phantom is placed at the origin $\boldsymbol{r}_1 = \boldsymbol{0}$ of the robot coordinate system and a series of 4000 Lissajous cycles is measured. In a second experiment, the single-marker-phantom is moved to 100 positions within the drive field field of view. The positions were chosen randomly prior to the experiment. At each position, a series of 100 cycles is measured. In the last experiment the three-marker-phantom is moved to 100 positions in such that all markers were located inside the field of view during the entire measurement series. Again, the positions were chosen at random prior to the experiment, and a series of 100 MPI measurements was obtained at each position.

III. Results

III.I. Experiment 1: Systematic Error and Statistical Error

From the first experiment, a sequence of 4000 tomograms was obtained, from which the single marker center of mass positions and the corresponding localization errors $\boldsymbol{\delta}_1(t_i)$, $1 \le i \le 4000$ were computed for 101 equidistantly-spaced relative segmentation thresholds

Θ	$\mu_1^x \pm \sigma_1^x$ [mm]	$\mu_1^y \pm \sigma_1^y$ [mm]	$\mu_1^z \pm \sigma_1^z$ [mm]
0.1	0.04 ± 0.02	0.05 ± 0.02	-0.02 ± 0.01
0.3	0.02 ± 0.02	0.07 ± 0.04	-0.07 ± 0.02
0.5	-0.01 ± 0.04	0.05 ± 0.03	-0.05 ± 0.02
0.7	0.02 ± 0.02	0.06 ± 0.07	0.07 ± 0.02
1.0	0.36 ± 0.30	-0.19 ± 0.29	0.10 ± 5.34

Table 2: Estimates of the systematic and the corresponding statistical localization error $\boldsymbol{\mu}_1$ and $\boldsymbol{\sigma}_1$ for several relative thresholds and the first experiment using the single-marker-phantom.

$\Theta \in [0,1]$. For $\Theta = 0.3$, the x-, y-, and z-component of the localization error are visualized in Fig. 5 for every 25th frame.

From $\boldsymbol{\delta}_1(t_i)$, the systematic and the statistical localization errors $\boldsymbol{\mu}_1$ and $\boldsymbol{\sigma}_1$ were estimated. A small fraction of these errors is given in Tab. 2 for relative thresholds $\Theta = 0.1$, 0.3, 0.5, 0.7, and 1.0. Our analysis shows that for all Θ there is a systematic deviation in the marker localization, which cannot be explained by the corresponding statistical error. An in depth analysis of the localization error $\boldsymbol{\delta}_1(t_i)$ reveals that the underlying distribution varies strongly with the relative threshold Θ. The distribution might be mono-modal as shown in Fig. 6a for $\Theta = 0.1$ or overlaying multi-modal in one or more components as can be seen in Fig. 6b for $\Theta = 0.3$.

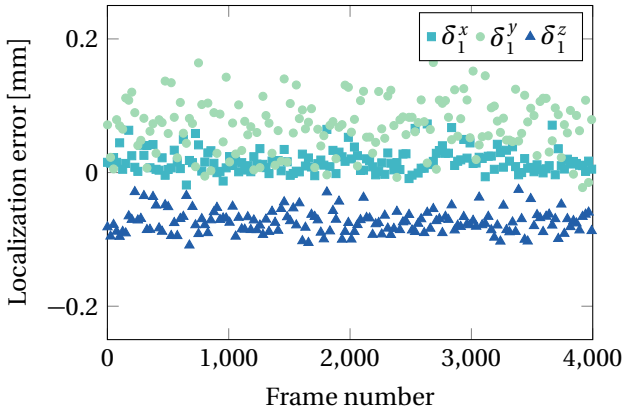

Figure 5: A scatter plot shows the localization error in x-, y-, and z-direction for the relative threshold $\Theta = 0.3$. For reasons of clarity, only every 25th point is plotted.

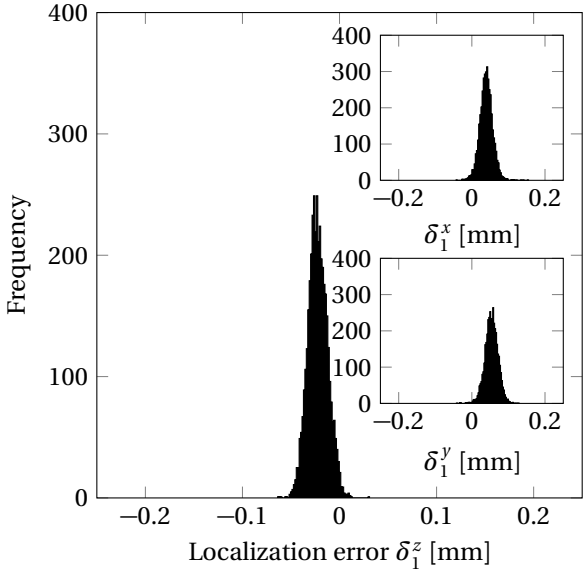

(a) Distribution of $\boldsymbol{\delta}_1$ for $\Theta = 0.1$.

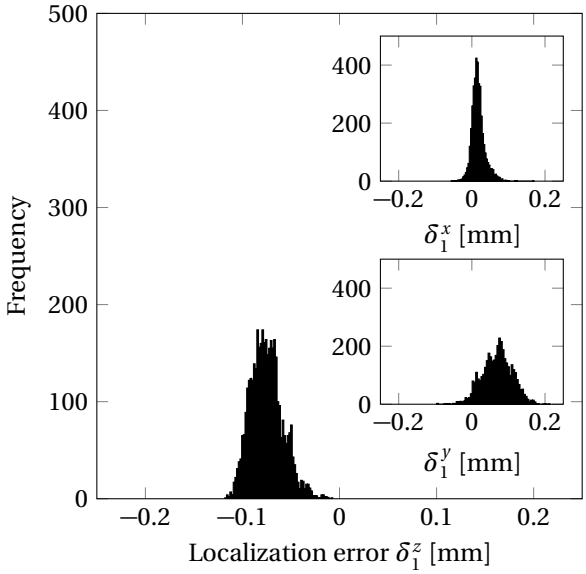

(b) Distribution of $\boldsymbol{\delta}_1$ for $\Theta = 0.3$.

Figure 6: These histograms show the distribution of the localization error within the first experiment for two relative thresholds Θ.

III.II. Experiment 2: Temporal and Spatial Dependence of the Systematic Error

From the second experiment, a data set of 100×100 frames was reconstructed, 100 frames at each random robot position $\boldsymbol{r}_m$, $1 \leq m \leq 100$. As in the first experiment, the single marker was localized and the corresponding localization error $\boldsymbol{\delta}_1$ was calculated for each frame using a relative threshold of $\Theta = 0.3$. The relative threshold was chosen heuristically and it ensures the comparability between Experiment 2 and 3. For a small fraction of 9 permille of frames, the automatic marker localization deviated from the ground truth position by more than 1 mm. A detailed analysis of these frames revealed a faulty recognition of the brightest pixel as the marker due to strong noise in these tomograms. These frames were

removed from the dataset and not taken into consideration for calculation of the statistics. Then, the systematic and statistical errors $\boldsymbol{\mu}_1(\boldsymbol{r})$ and $\boldsymbol{\sigma}_1(\boldsymbol{r})$ were estimated for each random position $\boldsymbol{r}_m$. Similar to the first experiment, the statistical error is small compared to the systematic deviation $\|\boldsymbol{\sigma}_1(\boldsymbol{r}_m)\|_2 \ll \|\boldsymbol{\mu}_1(\boldsymbol{r}_m)\|_2$. Henceforth, we will therefore focus on the systematic error $\boldsymbol{\mu}_1(\boldsymbol{r}_m)$.

At first, the $\boldsymbol{\mu}_1(\boldsymbol{r}_m)$ were ordered with respect to the data acquisition time, i.e. according to m as shown in Fig. 7. A large spread in the systematic deviation of the x-position $\mu_1^x(\boldsymbol{r}_m)$ and y-position $\mu_1^y(\boldsymbol{r}_m)$ was observed compared to the component $\mu_1^z(\boldsymbol{r}_m)$. In detail, the component-wise error bounds were $-0.42\,\text{mm} \leq \mu_1^x(\boldsymbol{r}_m) \leq 0.57\,\text{mm}$, $-0.38\,\text{mm} \leq \mu_1^y(\boldsymbol{r}_m) \leq 0.50\,\text{mm}$, and $-0.14\,\text{mm} \leq \mu_1^y(\boldsymbol{r}_m) \leq 0.17\,\text{mm}$, and the absolute systematic error was bounded by $\|\boldsymbol{\mu}_1\|_2 \leq 0.7\,\text{mm}$.

The total measurements took 400 s. Within our measurement data a minor temporal drift was observed. By binning the data into groups of 10 consecutive positions respectively, a systematic non linear drift of the mean of $\mu_1^z(\boldsymbol{r}_m)$ by about 0.15 mm was discovered throughout the entire measurement. The other components experienced no such significant temporal drift. Note that no correction of the temporal drift was performed.

Next, the spatial dependence of the systematic error $\boldsymbol{\mu}_1$ was investigated. Fig. 8 shows all three components of the systematic error plotted against the x-component of the robot position of the single-marker-phantom. Clearly, μ_1^x varies with the x-component, which provides an explanation for the larger spread in the time-ordered data in Fig. 7. To verify our assumption, our data set was split into two subsets. The first contains the data $\boldsymbol{c}_1, \boldsymbol{c}_3, \ldots, \boldsymbol{c}_{99}$ corresponding to odd numbered random positions $\boldsymbol{r}_1, \boldsymbol{r}_3, \ldots, \boldsymbol{r}_{99}$. The second contains the data corresponding to even numbered random positions. The first subset is used to fit a linear model $\boldsymbol{\mu}_1(\boldsymbol{c}) = A\boldsymbol{c} + \boldsymbol{b}$ to our data. We find that

$$A = \begin{pmatrix} 0.024 & 0 & 0 \\ 0 & -0.013 & 0 \\ 0 & 0 & 0 \end{pmatrix}, \boldsymbol{b} = \begin{pmatrix} 0.06\,\text{mm} \\ 0.06\,\text{mm} \\ 0.00\,\text{mm} \end{pmatrix}, \quad (7)$$

where all coefficients obtained from linear regression with an absolute t-value less than 3.2 were set to zero. Note that the standard deviation of the coefficients in A and $\boldsymbol{b}$ is of the order of the last digit provided.

Applying the linear model as a first-order correction to the marker localization $\boldsymbol{c}_k \mapsto \boldsymbol{c}_k + A\boldsymbol{c}_k + \boldsymbol{b}$ to the second subset, we find that the systematic error for the corrected data drops considerably. In this case, the error bounds for the component-wise errors were reduced to $-0.20\,\text{mm} \leq \mu_1^x(\boldsymbol{r}_m) \leq 0.34\,\text{mm}$, $-0.20\,\text{mm} \leq \mu_1^y(\boldsymbol{r}_m) \leq 0.25\,\text{mm}$, and $-0.11\,\text{mm} \leq \mu_1^y(\boldsymbol{r}_m) \leq 0.12\,\text{mm}$, and for the absolute systematic error to $\|\boldsymbol{\mu}_1\|_2 \leq 0.4\,\text{mm}$. Cross-validation of the linear model using the second corrected data set yielded no coefficients with absolute t-value above 3.2.

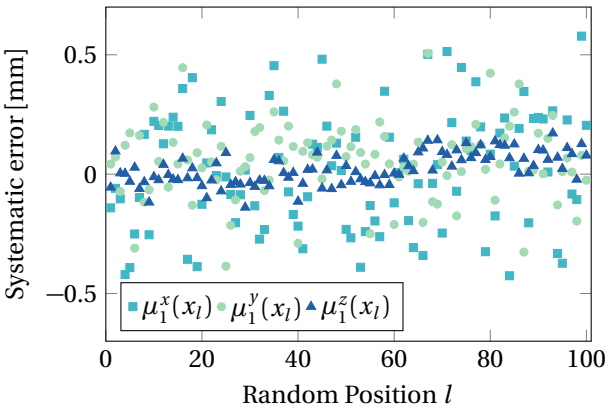

Figure 7: The systematic error ordered with respect to time. During the second experiment, the robot was moved to the random positions $\boldsymbol{r}_m$.

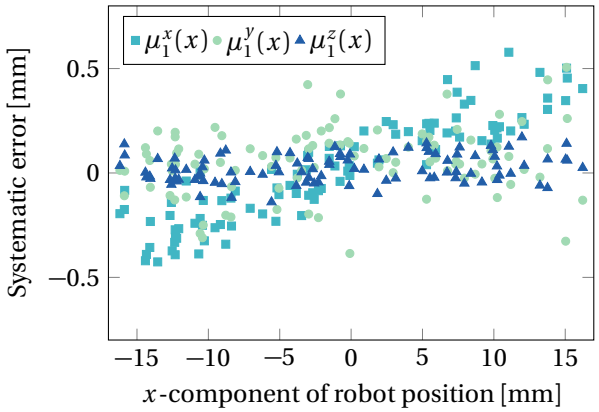

Figure 8: The three spatial components of the systematic error μ_1^x, μ_1^y and μ_1^z are ordered with respect to the x-component of the robot position of the single-marker-phantom. One observes a strong correlation between μ_1^x and x.

III.III. Experiment 3: Localization of Multiple Markers in a Multi-Marker Phantom

In the last experiment, the multi-marker phantom was positioned at 100 randomly generated positions $\boldsymbol{r}_m$, $1 \leq m \leq 100$ chosen such that the all markers were inside the field of view during the entire experiment. As in the last experiment, 100 frames $1 \leq p \leq 100$ were measured at each random position. Similar to the last experiment, the position of each marker $\boldsymbol{c}_1(m,p)$, $\boldsymbol{c}_2(m,p)$, and $\boldsymbol{c}_3(m,p)$ was obtained for the p-th tomogram measured at position $\boldsymbol{r}_m$ for a relative threshold of $\Theta = 0.3$. For this particular experiment the choice of Θ is restricted. For too small values, e.g. $\Theta = 0.1$, the markers c1 and c2 are indistinguishable by our simple computer vision algorithm.

The marker positions were used to obtain estimates of

the marker distances $d_{12}(m,p) = \|\boldsymbol{c}_1(m,p) - \boldsymbol{c}_2(m,p)\|_2$, $d_{13}(m,p) = \|\boldsymbol{c}_1(m,p) - \boldsymbol{c}_3(m,p)\|_2$, and $d_{23}(m,p) = \|\boldsymbol{c}_2(m,p) - \boldsymbol{c}_3(m,p)\|_2$ for each tomogram as shown in Fig. 9. We did apply the corrections of the marker position obtained in the second experiment prior to the distance estimations.

A closer analysis reveals that the multi-marker phantom was not correctly recognized in a fraction of 2 permille of the tomograms. Here, the multi-marker phantom was interpreted as correctly recognized if none of the distance estimates deviate by more than 1 mm from the ground truth distances given in Tab. 1. We found that a faulty recognition is mainly caused by our localization algorithm, which sorts the initially identified high-intensity connected components with respect to their brightest pixel while assuming the markers correspond to these connected components. In a small fraction of the tomograms, a noise pixel was falsely identified as marker. With these outliers removed from our dataset, we find that the marker distances are estimated to an average of $d_{12} = 9.6 \pm 0.3$mm (9.6 ± 0.3mm), $d_{13} = 17.1 \pm 0.3$mm (17.3 ± 0.3mm), and $d_{23} = 14.3 \pm 0.3$mm (14.3 ± 0.3mm), which is in good agreement with the estimates from the 3D CAD drawing of our phantom which are shown in Tab. 1. The marker distances in brackets are not corrected with the linear model. The reconstructed 3D tomogram of the multi-marker phantom and its maximum intensity projections can be seen in Fig. 10.

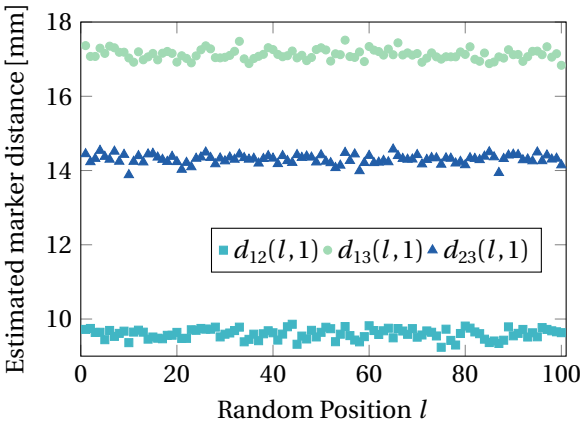

Figure 9: A scatter plot shows the estimated marker distances of the multi-marker phantom. For reasons of clarity, only estimates from the first frame recorded at a random position are shown.

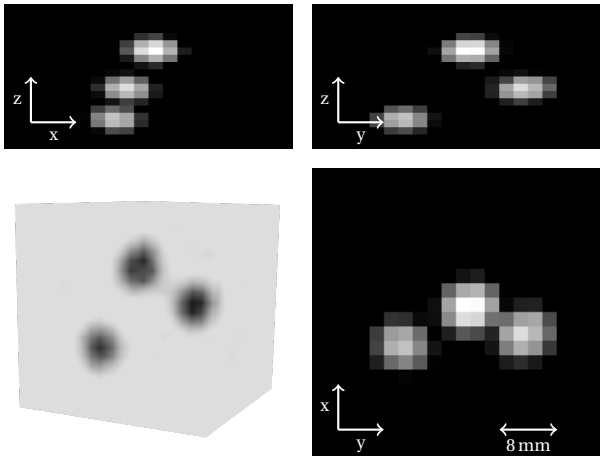

Figure 10: A reconstructed 3D tomogram of the multi-marker phantom is shown as a maximum intensity projection for the *xz*-, *yz*- and *xy*-plane. In the lower left image the 3D tomogram is depicted as 3D rendering. The estimated marker distances are $d_{12} = 9.6 \pm 0.3$mm, $d_{13} = 17.1 \pm 0.3$mm and $d_{23} = 14.3 \pm 0.3$mm.

IV. Discussion and Conclusion

We provided a proof of principle that automatic and reliable marker localization within a time series of MPI tomograms measured at a rate of 46 tomograms per second is possible.

Recall that our system was operated at a low field gradient of 1.5 T m^{-1} in z-direction and 0.75 T m^{-1} in x- and y-direction as well as a drive field amplitude of 14 mT. From our image data, we estimated the spatial resolution of the reconstructed MPI tomograms to be 6.0 mm, 7.1 mm, and 2.9 mm. The analysis of our second experiment revealed that a submillimeter-accurate localization with an accuracy of about ±0.27 mm in x- and y-direction and ±0.12 mm in z-direction can be achieved. This marks a more than 10-fold increase compared to the spatial resolution of our MPI system.

As our MPI tomograms contain some noise the very basic marker recognition used here infrequently identifies noise voxels as marker. Overall, however, the marker recognition has proved to be very robust. The recognition failure rate for the single-marker is only 9 permille and only 2 permille for a multi-marker phantom containing three markers. The underlying noise is likely to originate from our MPI scanner hardware. To compensate faulty recognition one could either recognize these noisy frames by a noise analysis or use more stable algorithms like template matching for marker localization.

The localization algorithm used in this work depends on a threshold parameter Θ. The choice of Θ was mainly limited by the multi-marker phantom, where markers could no longer be discriminated for small values. Hence the parameter was chosen heuristically to be $\Theta = 0.3$ around which its influence on the localization result was very small. However, this parameter is algorithm specific and hence can be avoided by using more sophisticated computer vision algorithms.

A detailed analysis of the of the systematic localization error revealed a small non linear temporal drift and spatial dependence of this error. First order corrections

10.18416/ijmpi.2017.1703011

of the spatial dependence could significantly reduce the systematic localization error down to 0.4 mm. Possible sources of this error could be slight differences in the thermal or magnetic state of the MPI scanner during system matrix acquisition and marker measurements. In order to gain confidence in the automated marker localization further investigations of this issue are required. Though, even without a correction of these temporal and spatial deviations the main result of our work remains valid.

Although in the current study marker localization has been performed off-line, i.e. after data acquisition, real-time marker localization is feasible since the marker localization took about 1.3 ms per frame compared to the 21.54 ms cycle lenght per frame. Therefore, we believe that an automatic submillimeter-accurate marker localization at high temporal resolutions will be useful for medical real-time applications such as device tracking and navigation, which would otherwise be limited by the low spatial resolution of MPI. Using MPI for human real-time applications, the size of the field of view will be a limited due to the drive field strength exceeding the safety constraints of the peripheral nerve stimulation (PNS) [26]. With higher excitation frequencies the safety constraints of the PNS can be extended but then the specific absorption rate (SAR) becomes a limiting factor [27]. This might restrict the usage of MPI in e.g. interventional applications. To circumvent these limitations, an automatic instrument localization can be used to continuously shift the field of view to follow the instrument movement. A robust instrument localization algorithm as proposed in this work is essential within such a real-time imaging setup.

Acknowledgment

The authors thankfully acknowledge the financial support by the German Research Foundation (DFG, grant numbers KN 1108/2-1 and AD 125/5-1).

References

[1] B. Gleich and J. Weizenecker. Tomographic imaging using the nonlinear response of magnetic particles. *Nature*, 435(7046):1214–1217, 2005. doi:10.1038/nature03808.

[2] J. Weizenecker, B. Gleich, J. Rahmer, H. Dahnke, and J. Borgert. Three-dimensional real-time in vivo magnetic particle imaging. *Phys. Med. Biol.*, 54(5):L1–L10, 2009.

[3] J. Rahmer, A. Antonelli, C. Sfara, B. Tiemann, B. Gleich, M. Magnani, J. Weizenecker, and J. Borgert. Nanoparticle encapsulation in red blood cells enables blood-pool magnetic particle imaging hours after injection. *Phys. Med. Biol.*, 58(12):3965, 2013. doi:10.1088/0031-9155/58/12/3965.

[4] B. Zheng, T. Vazin, P. W. Goodwill, A. Conway, A. Verma, E. U. Saritas, D. Schaffer, and S. M. Conolly. Magnetic Particle Imaging tracks the long-term fate of in vivo neural cell implants with high image contrast. *Sci. Rep.*, 5:14055, 2015. doi:10.1038/srep14055.

[5] B. Zheng, M. P. von See, E. Yu, B. Gunel, K. Lu, T. Vazin, D. V. Schaffer, P. W. Goodwill, and S. M. Conolly. Quantitative Magnetic Particle Imaging Monitors the Transplantation, Biodistribution, and Clearance of Stem Cells In Vivo. *Theranostics*, 6(3):291–301, 2016. doi:10.7150/thno.13728.

[6] K. Them, J. Salamon, P. Szwargulski, S. Sequeira, M. G. Kaul, C. Lange, H. Ittrich, and T. Knopp. Increasing the sensitivity for stem cell monitoring in system-function based magnetic particle imaging. *Phys. Med. Biol.*, 61(9):3279–3290, 2016. doi:10.1088/0031-9155/61/9/3279.

[7] W. R. Brody. Digital Subtraction Angiography. *IEEE Trans. Nucl. Sci.*, 29(3):1176–1180, 1982. doi:10.1109/TNS.1982.4336336.

[8] J. Haegele, J. Rahmer, B. Gleich, J. Borgert, H. Wojtczyk, N. Panagiotopoulos, T. M. Buzug, J. Barkhausen, and F. M. Vogt. Magnetic Particle Imaging: Visualization of Instruments for Cardiovascular Intervention. *Radiology*, 265(3):933–938, 2012.

[9] T. Knopp and M. Hofmann. Online reconstruction of 3D magnetic particle imaging data. *Phys. Med. Biol.*, 61(11):N257–N267, 2016. doi:10.1088/0031-9155/61/11/N257.

[10] J. Salamon, M. Hofmann, C. Jung, M. G. Kaul, F. Werner, K. Them, R. Reimer, P. Nielsen, A. vom Scheidt, G. Adam, T. Knopp, and H. Ittrich. Magnetic Particle / Magnetic Resonance Imaging: In-Vitro MPI-Guided Real Time Catheter Tracking and 4D Angioplasty Using a Road Map and Blood Pool Tracer Approach. *PLOS ONE*, 11 (6):e0156899, 2016. doi:10.1371/journal.pone.0156899.

[11] J. Haegele, S. Cremers, J. Rahmer, J. Franke, S. Vaalma, M. Heidenreich, J. Borgert, P. Borm, J. Barkhausen, and F. M. Vogt. Magnetic Particle Imaging: A Resovist based Marking Technology for Guide Wires and Catheters for Vascular Interventions. *IEEE Trans. Med. Imag.*, 35(10):2312–2318, 2016. doi:10.1109/TMI.2016.2559538.

[12] J. Rahmer, A. Halkola, B. Gleich, I. Schmale, and J. Borgert. First experimental evidence of the feasibility of multi-color magnetic particle imaging. *Phys. Med. Biol.*, 60(5):1775–1791, 2015. doi:10.1088/0031-9155/60/5/1775.

[13] F. Werner, C. Jung, M. Hofmann, R. Werner, J. Salamon, D. Säring, M. G. Kaul, K. Them, O. M. Weber, T. Mummert, G. Adam, H. Ittrich, and T. Knopp. Geometry planning and image registration in magnetic particle imaging using bimodal fiducial markers. *Med. Phys.*, 43(6):2884–2893, 2016. doi:10.1118/1.4948998.

[14] R. M. Ferguson, A. P. Khandhar, S. J. Kemp, H. Arami, E. U. Saritas, L. R. Croft, J. Konkle, P. W. Goodwill, A. Halkola, J. Rahmer, J. Borgert, S. M. Conolly, and K. M. Krishnan. Magnetic Particle Imaging With Tailored Iron Oxide Nanoparticle Tracers. *IEEE Trans. Med. Imag.*, 34(5):1077–1084, 2015. doi:10.1109/TMI.2014.2375065.

[15] M. Graeser, K. Bente, and T. M. Buzug. Dynamic single-domain particle model for magnetite particles with combined crystalline and shape anisotropy. *J. Phys. D: Appl. Phys.*, 48(27):275001, 2015. doi:10.1088/0022-3727/48/27/275001.

[16] J. Weizenecker, B. Gleich, J. Rahmer, and J. Borgert. Micromagnetic simulation study on the magnetic particle imaging performance of anisotropic mono-domain particles. *Phys. Med. Biol.*, 57(22):7317–7327, 2012. doi:10.1088/0031-9155/57/22/7317.

[17] J. Rahmer, J. Weizenecker, B. Gleich, and J. Borgert. Analysis of a 3-D System Function Measured for Magnetic Particle Imaging. *IEEE Trans. Med. Imag.*, 31(6):1289–1299, 2012. doi:10.1109/TMI.2012.2188639.

[18] P. W. Goodwill and S. M. Conolly. The x-Space Formulation of the Magnetic Particle Imaging process: One-Dimensional Signal, Resolution, Bandwidth, SNR, SAR, and Magnetostimulation. *IEEE Trans. Med. Imag.*, 29(11):1851–1859, 2010. doi:10.1109/TMI.2010.2052284.

[19] P. Vogel, M. A. Rückert, P. M. Jakob, and V. C. Behr. μ MPI - Initial Experiments With an Ultrahigh Resolution MPI. *IEEE Trans. Magn.*, 51(2):6502104, 2015. doi:10.1109/TMAG.2014.2329135.

[20] J. Rahmer, J. Weizenecker, B. Gleich, and J. Borgert. Signal encoding in magnetic particle imaging: properties of the system function. *BMC Medical Imaging*, 9(4), 2009. doi:10.1186/1471-2342-9-4.

[21] T. Knopp, S. Biederer, T. F. Sattel, M. Erbe, and T. M. Buzug. Prediction of the Spatial Resolution of Magnetic Particle Imaging Using the Modulation Transfer Function of the Imaging Process. *IEEE Trans. Med. Imag.*, 30(6):1284–1292, 2011. doi:10.1109/tmi.2011.2113188.

[22] M. Y. Wang, C. R. Maurer, J. M. Fitzpatrick, and R. J. Maciunas. An automatic technique for finding and localizing externally attached markers in CT and MR volume images of the head. *IEEE Trans. Biomed. Eng.*, 43(6):627–637, 1996. doi:10.1109/10.495282.

[23] T. Knopp, J. Rahmer, T. F. Sattel, S. Biederer, J. Weizenecker, B. Gleich, J. Borgert, and T. M. Buzug. Weighted iterative reconstruction for magnetic particle imaging. *Phys. Med. Biol.*, 55(6):1577–1589, 2010. doi:10.1088/0031-9155/55/6/003.

[24] J.-P. Fillard. Subpixel accuracy location estimation from digital signals. *Opt. Eng.*, 31(11):2465–2471, 1992. doi:10.1117/12.59956.

[25] J. Rauschenberg, A. de Oliveira, S. Müller, W. Semmler, and M. Bock. An algorithm for passive marker localization in interventional MRI. *Z. Med. Phys.*, 17(3):180–189, 2007.

[26] E. U. Saritas, P. W. Goodwill, G. Z. Zhang, and S. M. Conolly. Magnetostimulation Limits in Magnetic Particle Imaging. *IEEE Trans. Med. Imag.*, 32(9):1600–1610, 2013. doi:10.1109/TMI.2013.2260764.

[27] I. Schmale, B. Gleich, J. Schmidt, J. Rahmer, C. Bontus, R. Eckart, B. David, M. Heinrich, O. Mende, O. Woywode, J. Jokram, and J. Borgert. Human PNS and SAR study in the frequency range from 24 to 162 kHz. In *International Workshop on Magnetic Particle Imaging*, 2013. doi:10.1109/IWMPI.2013.6528346.

